Charging kinetics of a vibrated bed of particles by numerical simulations and experiments

Komlanvi Lampoh, Farhang Radjai, Claire Mayer-Laigle, Xavier Rouau, Jean-Yves Delenne

Charging kinetics of a vibrated bed of particles by numerical simulations and experiments

Komlanvi Lampoh[a,*], Farhang Radjai[b], Claire Mayer-Laigle[a], Xavier Rouau[a], Jean-Yves Delenne[a]

[a] *IATE, University of Montpellier, INRAE, Institut Agro, Montpellier, France*
[b] *LMGC, University of Montpellier, CNRS, Montpellier, France*

Abstract

Through particle dynamics simulations and experiments, we investigate the charging kinetics of a granular bed in a vibrating cell. The numerical method is based on a theoretical model combining an equation for charge transfer at the particle scale with a theoretical model of charge relaxation. Simultaneously, experiments are carried out to calibrate and validate the numerical model using a vibrated cell with glass beads. Specific charge per unit mass induced by vibrations initially increases before leveling off. Saturation specific charge and charging characteristic time decrease with increasing bed mass. Data collapse onto a master curve is observed when normalizing specific charges and times. At the particle scale, we find that charge saturation results from the balance between charge transfer and relaxation. Saturation specific charge correlates with the relative rate of collisions between particles and the vibrating plate. We introduce a simple expression for the average ballistic time based on single-particle dynamics and a restitution coefficient dependent on bed mass. The characteristic time is proportional to the ballistic time and decreases with increasing bed mass due to more inelastic collisions between particles.

Keywords: triboelectric charge, electrostatic experiments, Discrete Element Method, granular materials
PACS: 45.70.Mg, 61.43.Gt
2000 MSC: 76T25, 74F15, 78M25

*komlanvi.lampoh@inrae.fr

1. Introduction

The handling of powders is crucial for the formulation of many products such as foods, pharmaceuticals, cosmetics, civil engineering materials, and particle embedded composites. In addition to the inherent complexity of granular media, electrostatic charges due to particle-particle or particle-surface contacts generate attractive and repulsive forces that deeply modify the mechanical behavior of powders. These interactions are at the origin of technological issues related to the handling of powders such as agglomeration effects, clogging and adhesion to surfaces. For example, electrostatic forces are critical in space missions since their effects are enhanced by low gravity and lack of moisture [1, 2]. Electrostatic discharge can occur due to charge accumulation causing explosions of silos or flour mills [3, 4]. On the contrary, these interactions can also be exploited in processes. Well known examples are electrostatic separation [5, 6], coating [7, 8], and powder inks for laser printers [9].

Although all particle flows can give rise to triboelectric charges, the exchanged charge level strongly depends on the materials used and their relative position in the triboelectric series [10]. The charge migration process in the system is driven by the particle collision dynamics. For this reason, highly dynamic processes such as vibrated or fluidized beds, which are widely used in industrial processes for drying, mixing, and sorting, are strongly affected by electrostatic interactions [11, 12, 13].

Triboelectric charging can occur by electron or ionic transfer or due to a transport of material. Several theoretical models have been introduced based on these different types of charge transfer. However, the underlying physical phenomenon remains poorly understood [4]. The most detailed approaches such as quantum simulations [14] or models based on the distribution of electrons according to Fermi energy [15] directly consider the atomic scale but are hardly usable at the grain scale. Indeed, charging may also depend on grain scale characteristics such as their size, surface roughness, and mechanical loading [16, 17]. Furthermore, environmental factors such as humidity and temperature influence the characteristic time of return to electrostatic neutrality [18].

Several grain-scale phenomenological models have been proposed in the past [19, 20]. These models involve the so-called work function providing the minimal energy necessary to gain or lose an electron, and were introduced for the first time in the seminal paper of Gallo et al. [21]. This work function

should be calibrated experimentally. For example, the charging of a single sphere as a function of the number of collisions was investigated using various materials [22] and relative humidity and temperature [23].

To simulate the charging of a collection of particles, particle dynamics methods based on Discrete Element Models (DEM) can be efficiently used with the advantage of accounting for particle motions, interactions between particles, and collective effects such as arching, wall effects, force chains, and inelastic cooling. However, although most DEM-based simulations of electrostatic charging include a description of triboelectric charging at the particle scale based on the work function [24], they usually neglect the charge relaxation occurring during particle collisions. Various engineering applications were studied using DEM such as, for example, charge generation during mixing in vibrated granular beds [18, 25], triboelectric charging of particles rolling on inclined planes [26], and the pneumatic conveying [27].

In this paper, we focus on the modeling of triboelectric charging of a bed of particles subjected to vertical vibrations. This configuration is particularly important for the characterization of charging efficiency of a powder bed in contact with a plate of given material. We introduce a model of pairwise charge exchange between particles, which relies both on the equation of Laurentie et al. [24] for charge transfer and on the theoretical framework of Matsuyama and Yamamoto [28] for charge relaxation. We also calibrate and validate our numerical setting with experiments in bed charging under vertical vibrations. As we shall see, charge relaxation plays a key role in triboelectric charging. We apply this model to investigate the evolution of the specific charge for increasing bed mass and we analyze the origins of the saturation charge and and charging rate at the particle scale.

In the following, we first briefly describe in Section 2 the principles of the implementation of our DEM-based model for electric field and triboelectric charging. Then, we present in Section 3 our experimental electrostatic charging setup and tests performed on granular beds of different masses in order to calibrate the physical parameters of the numerical model. Section 3 describes the results of experiments performed to validate the charging kinetics for different masses of granular beds. A detailed numerical parametric study is presented with a broad range of values of granular bed mass. The calibrated numerical model is then used in Section 4 to investigate the charging kinetics for increasing bed mass. In Section 5, we introduce a scaling of the charging curves and a simple model based on single-particle assumption to clarify the role of particle-particle and particle-plate collision dynamics on

the charging regimes. We conclude with a summary of the main findings of this work and its possible extensions.

2. Modeling of triboelectric charging of particles

In this section, we describe our numerical model of particle charging. We first detail the theoretical model of charge transfer at the contact scale. Then, we propose an implementation of this model in the framework of the code that we developed for the simulations based on the Discrete Element Method (DEM).

2.1. Charge transfer at contact scale

Matsuyama and Yamamoto [28] proposed one of the first models of particle electrification due to contact and collisions. In this model, it is assumed that charge transfer between two particles i and j occurs only when they undergo a mechanical contact and it depends on a characteristic length δ_c called tunneling distance, which defines their maximum interaction distance. The particle pair behaves as a capacitor in which the electric charges are transferred by tunneling effect from one surface to the other. For simple shapes such as spheres, the corresponding surface of transfer S is explicitly known through the contact force law. To account for material properties such as chemical composition, particle size, and surface state, Matsuyama and Yamamoto used the so-called work function introduced in the earlier seminal paper of Gallo et al. [21]. The work function ϕ is the minimal energy necessary to extract one electron from an initially chargeless surface. It was theoretically evaluated for spherical particles [21]. In experiments, ϕ can be determined by photoemission [29] and Atomic Force Microscopy [30].

In the absence of an external electric field, for two particles i and j with different materials, the increment of charge gained or lost per unit time during a collision is [31, 32]

$$\frac{\Delta q_{ij}}{\Delta t} = C_{ij}(\phi_i - \phi_j), \tag{1}$$

with [24]

$$C_{ij} = \frac{\epsilon_r \epsilon_0}{4\pi\delta_c} \frac{\Delta S_{ij}}{\Delta t}, \tag{2}$$

where $\Delta S_{ij}/\Delta t$ is the contact area change rate, e is the absolute value of the electron charge, ϵ_0 is the dielectric constant of void, and δ_c is the tunneling distance between two particles for charge transfer. This model makes it

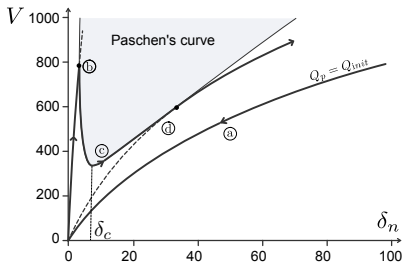

Figure 1: Paschen's limit curve describing the electric potential V necessary to initiate charge relaxation as a function of the gap δ_n. The bold line illustrates variation of electric potential for a pair of particles before (a) and after (b–d) the creation of mechanical contact leading to a variation of charge. The dashed line represents the variation of electric potential after charge relaxation.

possible to predict the evolution of the electric potential as a function of particle positions and to take into account the effect of their initial charge.

In the presence of an electric field $\vec{\mathsf{E}}_c$ due to particle charges or an external potential, following the work of Laurenti et al [24], the model of charge transfer can be written as:

$$\begin{cases} \Delta q_{ij}^t = \Delta S_{ij} \frac{\varepsilon_0}{\delta_c e} (\Delta \phi_{ij} - \vec{\mathsf{E}}_c \cdot \vec{n}_{ij} \delta_c e) & \text{if } \Delta S_{ij} > 0, \\ \Delta q_{ij} = 0 & \text{if } \Delta S_{ij} \leq 0, \end{cases} \tag{3}$$

in which $\vec{n}_{ij}$ is the normal unit vector from particle j to particle i. For spheres, the contact surface area can be approximated as [33]:

$$S_{ij} = \pi R^\star \delta_{n_{ij}} \tag{4}$$

where $R^\star = \frac{2}{1/R_i + 1/R_j}$. Hence, the variation of contact area is proportional to that of δ_n.

In addition to charge transfer due to potential difference, we need a model for charge relaxation due to micro-discharges (electric arcs). In the literature, this effect has been modeled in different ways. For example, Chen et al. [34] considered that the electric charge undergoes an exponential decrease with time $q(t)/q_\infty = 1 - e^{-(1/\tau+\beta)t}$ where q_∞ is the maximal sustainable charge, and τ and β are relaxation parameters describing the charge transfer and the effect of environmental conditions, respectively. Mastsuyama and Yamamoto [22] assumed that micro-discharges occur when the gap between two surfaces is close to the tunneling distance δ_c. This process is described by Paschen's curve, which gives the maximum potential that can sustain the surrounding

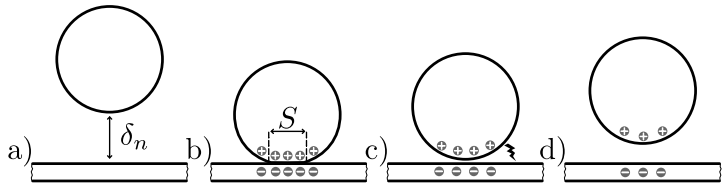

Figure 2: Illustration of a particle (a) coming into contact with a wall and gaining electric charge during deformation (b). Micro-discharges occurs in the vicinity of contact for distances ranging from a few nanometers to micrometers (c) and move apart with a residual charge (d).

gas before a discharge occurs, as shown in Fig. 1. In this figure, we assume that when a particle impacts a wall (or two particles collide), as illustrated in Fig. 2, different steps should be distinguished:

1. A particle of charge $q_p = q_0$ (where q_0 is the initial charge) is approaching a wall. As the difference of potential is proportional to the difference of charges between the particle and the wall, ΔV is independent of δ_n at large δ_n. However, as the gap declines, the potential decreases and eventually vanishes when the particle touches the plane [35].
2. During collision, charges are exchanged between the two materials, leading to a sudden increases of $|q_p|$. After collision, the particle moves away and the potential ΔV between the particle and the plane increases.
3. When ΔV reaches the Paschen's limit curve, the charge relaxes due to micro-discharges.
4. The particle moves away with a residual charge, which can be above the initial charge (Fig. 2). Note that the minimum of the Paschen curve occurs at the distance δ_c.

The charge relaxation occurs over the characteristic distance δ_c. In the model of [22] the relaxation due to charge transfer through gas molecules is assumed to be negligible compared to electric arc discharges. In this work, we assume that charge transfer due to relaxation takes place only during the separation phase; see Fig. 2c. We use a linear relaxation rule with the parameter K_r defined by

$$\Delta q_{ij}^r = -K_r(q_i - q_j). \tag{5}$$

Although experimentally the charge density at the surface of a particle may be inhomogeneous [20], considering a nonuniform charge distribution

at the surface of each particle would lead to prohibitive computation time in 3D. For this reason, in this work we assume that particles are uniformly charged. For a particle i with contacts $j \in \mathcal{C}_i$, where $\mathcal{C}_i$ is the set of particles in electric contact with i, the charge of the particle at time $t + dt$ is given by

$$q_i(t + dt) = q_i(t) + \sum_{j \in \mathcal{C}_i} (\Delta q_{ij}^t + \Delta q_{ij}^r) \tag{6}$$

2.2. DEM implementation

For the simulations, we used the Discrete Element Method (DEM) [36, 37, 38] by adding the electrostatic forces to frictional contact interactions between particles. For time integration of the equations of motion of the particles the velocity-Verlet scheme was used [39]. At each time step, the forces and moments applied to all particles are calculated from particle positions and force laws. Then, using Newton's second law, the translational and angular accelerations of each particle are evaluated. Finally, using these accelerations and current velocities, the positions and velocities are updated.

The mechanical contact force is $\vec{F^c} = F_n^c \vec{n} + F_t^c \vec{t}$, where $\vec{n}$ and $\vec{t}$ are unit vectors defining the local reference frame at the contact between the two particles and F_n^c and F_t^c are its normal and tangential components; see Fig. 3. The normal component is given by the Hertz model

$$F_n^c = k_n \delta_n^{3/2} + \eta_n \vec{v}_{ij} \cdot \vec{n}, \tag{7}$$

where δ_n is the overlap distance, $\vec{v}_{ij} = \vec{v}_i - \vec{v}_j$, $k_n = \frac{4}{3} E^\star R^{\star 1/2}$ with $R^\star$ and $E^\star$ defined as the harmonic means of the radii and the moduli of the two particles, respectively, and η_n is the normal damping coefficient.

The tangential component is computed using a regularized Coulomb law

$$F_t^c = \min(k_t \delta_t - \eta_t ||\vec{v}_s||, \mu ||\vec{F}_n^c||), \tag{8}$$

where δ_t is the cumulative tangential displacement, η_t is the tangential damping coefficient, and

$$\vec{v_s} = (\vec{v}_{ij} - (\vec{v}_{ij} \cdot \vec{n}_{ij}) \vec{n}_{ij}) + (R_i \vec{\Omega}_i + R_j \vec{\Omega}_j) \wedge \vec{n} \tag{9}$$

is the sliding velocity and $k_t = 8 G^\star R_{ij}^{1/2}$ is the tangential stiffness with $G^\star$ defined as the effective shear modulus computed using an harmonic mean of the shear moduli of the two particles.

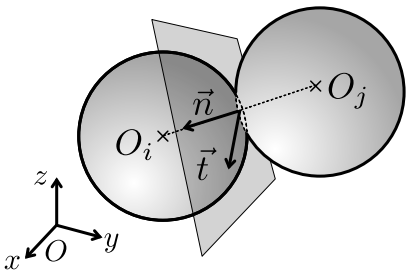

Figure 3: The geometry of a contact between two particles.

In addition to the mechanical contact forces acting on each particle i, the latter is subjected to gravity and electrostatic forces. The electrostatic force $\vec{F}_i^e = \vec{\mathcal{E}}_i q_i$ is calculated using the electric field at the center of mass of particle i:

$$\vec{\mathcal{E}}_i = \frac{1}{4\pi\epsilon_0} \sum_{j \neq i} \frac{q_j}{{r_{ij}}^2} \vec{n}. \tag{10}$$

The damping coefficients η_n and η_t can be scaled by the characteristic viscosities $\sqrt{m^\star k_n}$ and $\sqrt{m^\star k_t}$, respectively [40]. Therefore, we set

$$\eta_n = 2\alpha_n \sqrt{m^\star k_n}; \quad \eta_t = 2\alpha_t \sqrt{m^\star k_t} \tag{11}$$

The values of α_n and α_t are related to the normal and tangential restitution coefficients e_n and e_t, respectively [41]:

$$\alpha_n = \frac{\ln(e_n)}{\sqrt{\ln^2(e_n) + \pi^2}}; \quad \alpha_t = \frac{\ln(e_t)}{\sqrt{\ln^2(e_t) + \pi^2}} \tag{12}$$

Finally, in all simulations we set the time step $\Delta t = 10^{-6}$ s. With this value, the maximum gap δ_n in the system is below $3 \times 10^{-3} d$ and each collision involves at least 15 time steps. The CPU time for the simulation of charging of several hundred particles up to the maximum charge Q_∞ lasts from a few hours to four weeks on a moderate single-CPU station, depending on the number of particles. The simulation time is considerably longer here than in purely mechanical simulations (without electrostatic forces) mainly due to the calculation of the electrostatic field from particle charges in each time step. It is noteworthy that due to the strong inhomogeneity of particle charges during charging, it is not physically possible to cut off the electrostatic field below a few particle diameters.

3. Charging of a bed of particles

In this section, we present the principles of well-controlled experiments that we performed to calibrate and validate our triboelectric model. We first describe an in-house setup used to measure the evolution of the charge of a granular bed fluidized by means of a vibrating plate. These experiments together with DEM simulations will allow us to evaluate the tunneling distance δ_c and the relaxation coefficient K_r.

3.1. Experimental setup

The experiments are similar to those carried out by Liao et al. [13]. It consists of a bed of mass m_b of single-size glass beads placed on a a vibrating plate of given material, as schematized in Fig. 5(a). The particles are confined by a cylindrical box which vibrates with the plate. In this work, for all experiments we used polypropylene for the plate material. As compared to aluminium and PVC that we tested, polypropylene provides an efficient charge transfer since polypropylene and glass are well-separated in the triboelectric series based on the work function [42, 43]; see Fig. 4. Table 1 summarizes the material parameters of the glass beads and the polypropylene container.

The friction coefficient and normal restitution coefficient between the beads and with the container were determined experimentally. For friction a tripod of three beads glued on a piece of steal was used. At the beginning of the experiment, the tripod is placed on a glass or polypropilene plane. Then, the plane is gradually tilted until the tripod slides. From this angle the friction coefficient was found to be $\mu_b = 0.17 \pm 0.02$ for bead-bead and $\mu_p = 0.23 \pm 0.03$ bead-polypropilene contacts. This value of bead-bead friction coefficient is close to that ($\mu_b = 0.16$) measured elsewhere [45, 46]. Regarding the restitution coefficient, we used the classical method of free fall of a bead on a surface. We recorded the drop of particles using a high-frame camera and we determined the drop and rebound heights. We found a restitution coefficient of $e_b = 0.91 \pm 0.02$ for glass bead on glass surface and $e_p = 0.6 \pm 0.02$ for glass bead on polypropilene surface.

Let us note that all parameters required for DEM simulations using the electrostatic charging model are provided experimentally except the tunneling distance and relaxation coefficient, which are generally chosen arbitrarily in the literature [47, 24]. As we shall see below, we use the experimental data as compared with numerical simulations to adjust these parameters.

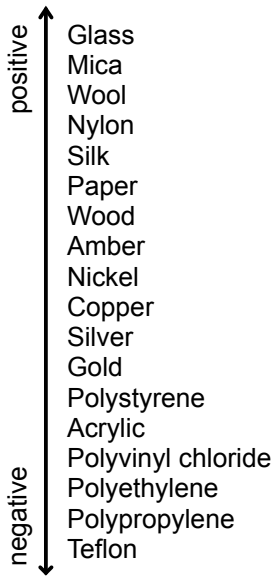

Figure 4: Typical example of triboelectric series adapted from [44].

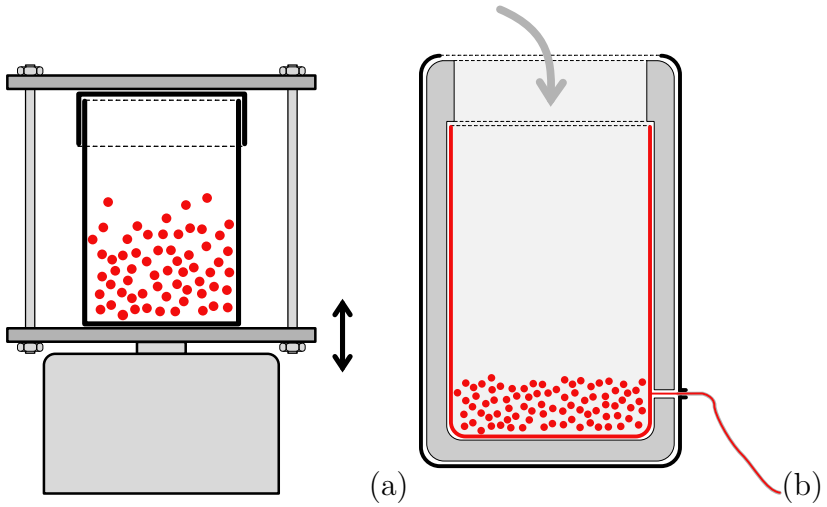

Figure 5: Schematic diagram of experimental setup with the vibrating system.

	Glass beads [48, 49]	Polypropilene box [50]
Young modulus (Pa)	$4.62\,10^{10}$	$1.3\,10^{9}$
Poisson coefficient	0.24	0.46
density ($\mathrm{kg\,m^{-3}}$)	2500	910
diameter (m)	0.002	0.05

Table 1: Material parameters for glass beads and polypropilene box.

The box is shaken using a Brünel & Kjær 4810 mini-shaker at a frequency ν =20 Hz with an amplitude A =1.5 mm. For these values, the relative acceleration is $A(2\pi\nu)^2/g \simeq 2.4$, leading to the fluidization of the granular bed across all its thickness. The vibration of the box is controlled by an amplified sinusoidal signal. The vibration amplitude was calibrated by means of a laser position sensor.

The total mass m_b of the beads and the vibration time t_v were varied and the bed charge was determined using and an electrometer and a Faraday cage; see Fig 5b). For each value of m_b and t_v, at least three independent measurements were performed. All experiments were carried out during a short period of time of the order of a few hours to avoid potential alteration of the results due to variations of humidity and temperature. The atmospheric conditions during experiments were a temperature of 26.5 ± 0.1°C and a humidity of $60 \pm 0.5\%$.

Figure 6 shows a typical example of the evolution of specific charge Q (charge per unit mass) as a function of time for $m_b = 1$ g. We see that Q first increases almost linearly at a rate $\dot{Q}_0$, and then slows down and tends to a steady-state value Q_∞ in a characteristic time τ. This steady-state specific charge is related to the maximum charge Q_{max} that a spherical particle can carry before the electrostatic field around the particle reaches the "breakdown field". It corresponds to the yield potential beyond which the air molecules are ionized and the particle charge is removed by the air charged ions. This theoretical limit can be approximated as $Q_{max} \simeq 2.64\,10^{-5} 4\pi R^2 p$, where $p = 3\epsilon_r/(\epsilon_r + 2)$ [15]. Using this semi-empirical relation, we find $Q_{max} \simeq 68$ $\mathrm{nC\,g^{-1}}$ which is of the same order of magnitude as $Q_\infty \simeq 21$ $\mathrm{nC\,g^{-1}}$ that we measured for a layer with $m_b = 1$ g of beads of diameter of 2 mm. In the following, we will use the theoretical value $Q_{max} = 68$ $\mathrm{nC\,g^{-1}}$ to normalize the specific charge.

To compare the experimental measurements with the numerical data, we apply numerically the same boundary conditions and vibrations in both

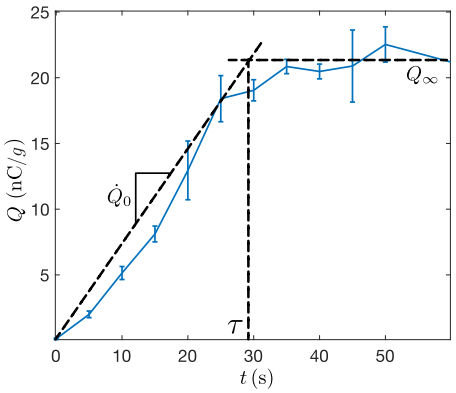

Figure 6: Evolution of specific charge Q as a function of time, illustrating the measured quantities: charging rate $\dot{Q}_0$, characteristic time τ, and asymptotic charge Q_∞.

cases. Regarding the tunneling distance and relaxation coefficient, a specific calibration procedure was necessary and it is described in the following section.

3.2. Determination of tunneling distance and relaxation coefficient

Little information can be found on the determination of the tunneling distance δ_c and relaxation coefficient K_r. The measurement of δ_c has been shown to be sensitive to surface properties such as roughness [51, 52]. Arbitrary values have been used for different powders, such as $\delta_c = 500$ nm for millimeter-sized polyamide particles [24] and $\delta_c = 250$ nm for a pharmaceutical powder [51]. Regarding K_r, to our best knowledge, no data are available since this parameter is not generally taken into account.

Figure 7 displays the evolution of the specific charge as a function of time for 1 g of particles and different values of δ_c and K_r. For a fixed value $K_r = 10^{-6}$ s^{-1} we varied gradually δ_c from 10 nm to 400 nm for 8 different values of δ_c. Ten values of K_r were also tested in the range from 10^{-7} s^{-1} to 5×10^{-6} s^{-1} for $\delta_c = 2 \times 10^{-7}$ m. Fig. 7(a) indicates that both the charging rate $\dot{Q}_0$ and saturation charge Q_∞ are strongly influenced by δ_c. On the contrary, Fig. 7(b) shows that K_r only controls the saturation charge, which decreases with increasing values of K_r.

Figure 8a shows the evolution of charging rate $\dot{Q}_0$ as a function of $1/\delta_c$. Interestingly, $\dot{Q}_0$ is proportional to $1/\delta_c$. This is consistent with Eq. (3) for weak values of $\vec{\mathsf{E}}_c$ at the beginning of the charging process. Hence, in the

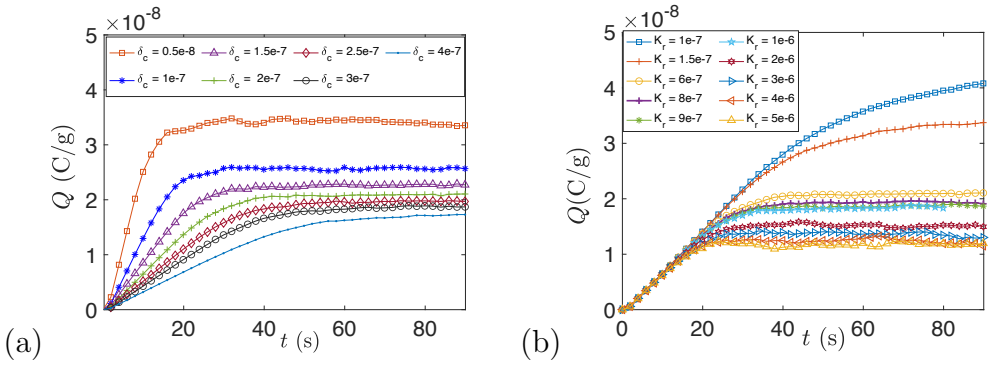

Figure 7: Evolution of the specific charge Q for a particle bed of mass equal to 1 g as a function of time for different values of the parameter δ_c (a) with $K_r = 10^{-6}$ s^{-1}, and K_r (b) for $\delta_c = 2\,10^{-7}$ m.

following we will assume

$$\dot{Q}_0(\delta_c) \simeq 1.50\,10^{-7}/\delta_c, \tag{13}$$

independently of K_r. From this equation and the experimental data of Fig. 6 (established for a granular bed of the same mass as as in simulations), we get $\delta_c \simeq 2\,10^{-7}$ m. For this value of δ_c, Fig. 8(b) shows that $\dot{Q}_0$ declines only very slightly with K_r so that its value can be considered to be practically constant.

We also consider the evolution of saturation charge $Q_\infty(\delta_c, K_r)$ as a function of δ_c shown in Fig. 9. We find a clear power-law dependence for both $Q_\infty(\delta_c, K_r = 10^{-6})$ and $Q_\infty(\delta_c = 2\,10^{-7}, K_r)$. Using the experimental value of $Q_\infty = 21.4$ nC for $m_b = 1$ g (Fig. 6) and the data of Fig. 9b, we get $K_r \simeq 6\,10^{-7}$ s^{-1}.

3.3. Effect of the bed mass

With the parameters calibrated in the case of $m_b = 1$ g, it is possible to simulate the charging of any amount of particles. Fig. 10(a) shows that our numerical simulations with the calibrated values of all parameters compare very well with the experimental data for bed masses of 2 g, 3 g and 4 g. Additional experiments were performed to evaluate the saturation charge Q_∞^{Exp} (for vibration time $t_v = 70$ s). Figures 10(b) and (c) show the experimental values of the saturation specific charge versus their numerical values Q_∞^{Sim} and as a function of the bed mass. We see that they agree well together up

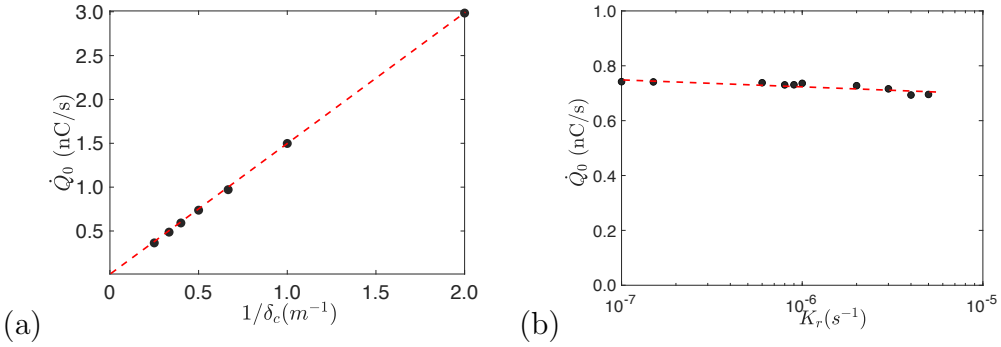

Figure 8: Charging rate for a granular bed of mass of 1 g (a) as a function of the inverse of tunneling distance $1/\delta_c$ with $K_r = 10^{-6}$ s^{-1} and its linear approximation $\dot{Q}_0 = 1.50\,10^{-7}/\delta_c$; (b) as a function of the relaxation parameter K_r for $\delta_c = 2\,10^{-7}$ m with its linear fit $\dot{Q}_0 = -1.36K_r + 0.75$ nC/s.

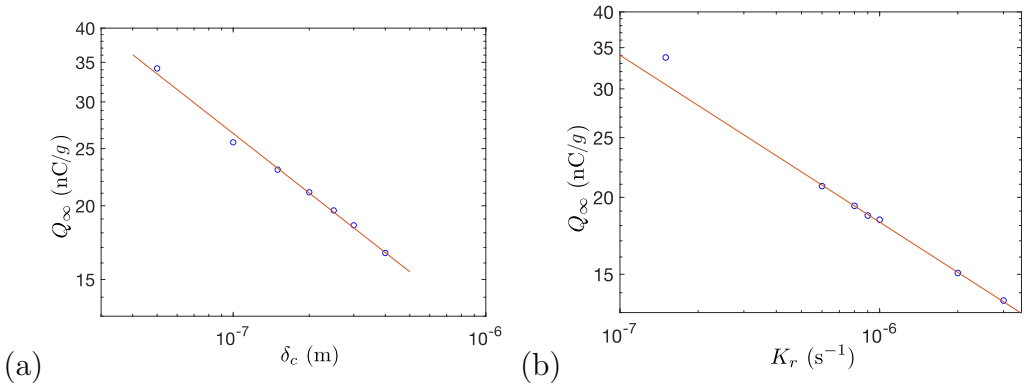

Figure 9: (a) Saturation charge as a function of tunneling distance from numerical simulations and its power-law fit $Q_\infty = 1.038\,10^{-10}\delta_c^{-0.335}$); (b) Saturation charge as a function of the relaxation parameter K_r from numerical simulations and its power-law fit $Q_\infty = 4.31\,10^{-10}K_r^{-0.271}$).

to a small systematic error, which may be attributed to the measurement method of the mass or saturation charge in experiments.

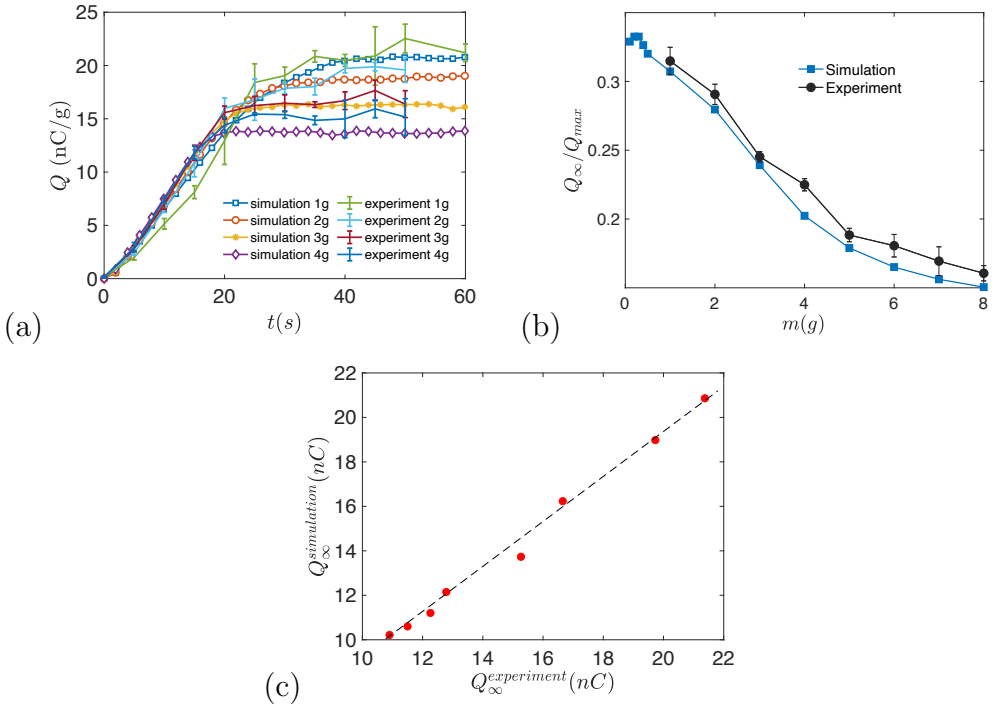

Figure 10: Comparison between experiments and simulations: (a) Specific charge (charge per unit mass) as a function of time for different values of bed mass; (b) Saturation charge as function of the bed mass m_b. The error bars represent standard deviation over three independent measurements in experiments; (c) Saturation charge obtained from numerical simulations versus their experimental values.

Finally, it is worth noting that, contrary to the work of Jari [53], who scaled the effective work function with mass, in our model the work function is an intrinsic parameter. However, its dependence on moister and temperature will have to be clarified in future works.

4. Charging kinetics

In this section, we use the calibrated numerical model described in the previous sections, to perform a detailed analysis of charging kinetics mainly as a function of the granular bed mass. Note that the influence of the bed mass has been considered in several previous studies, but no scaling has been

so far proposed [18, 24]. We performed a parametric study in which we varied the bed mass from 0.1 g to 8 g for a total number of 13 simulations. The number of particles varies from 100 to 1000. In each case, we simulated the charging kinetics up to 90 s. We first analyze below the charging process by distinguishing different mechanisms. Then, in the next section, we propose a general scaling of the charging kinetics.

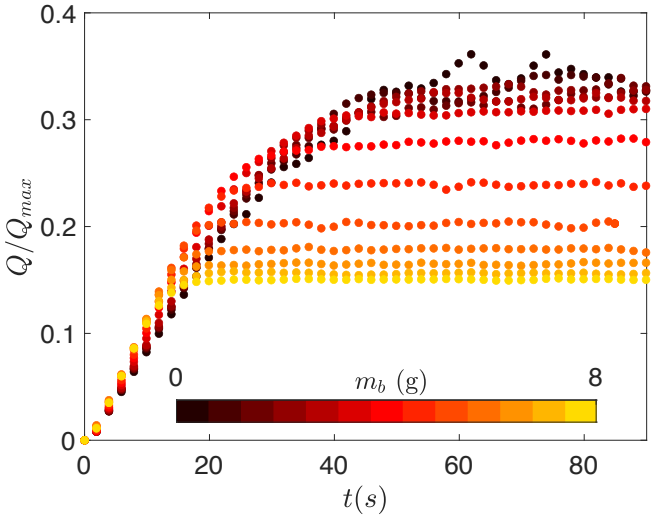

Figure 11: Specific charge Q normalized by Q_{max} as a function of time for different values of bed mass.

Figure 11 displays the charge ratio Q/Q_{max} as a function of time for all our simulations. Some of the same data were partially used in Fig. 10 for comparison with experiments. We see that, as shown previously, the total charge in the granular bed increases almost linearly with time at the beginning of the test and then tends to a constant asymptotic value Q_∞. As observed in Fig. 12(a), Q_∞ decreases slowly and in a nonlinear fashion with increasing bed mass m_b. Note that, while the specific mass declines with increasing mass m_b, the total saturation charge $Q_\infty m_b$ is an increasing function of m_b. This nonlinear dependence of Q_∞ on m_b seems to hold only for thin beds considered in this study since Q_∞ in Fig. 12(a) tends to a constant value with increasing m_b.

Figure 11 also shows that the initial charging rate $\dot{Q}_0$ per unit mass increases with m_b. This is what we observe in Fig. 12(b), which displays the initial charging rate as a function of m_b. The rate increases, but a transition

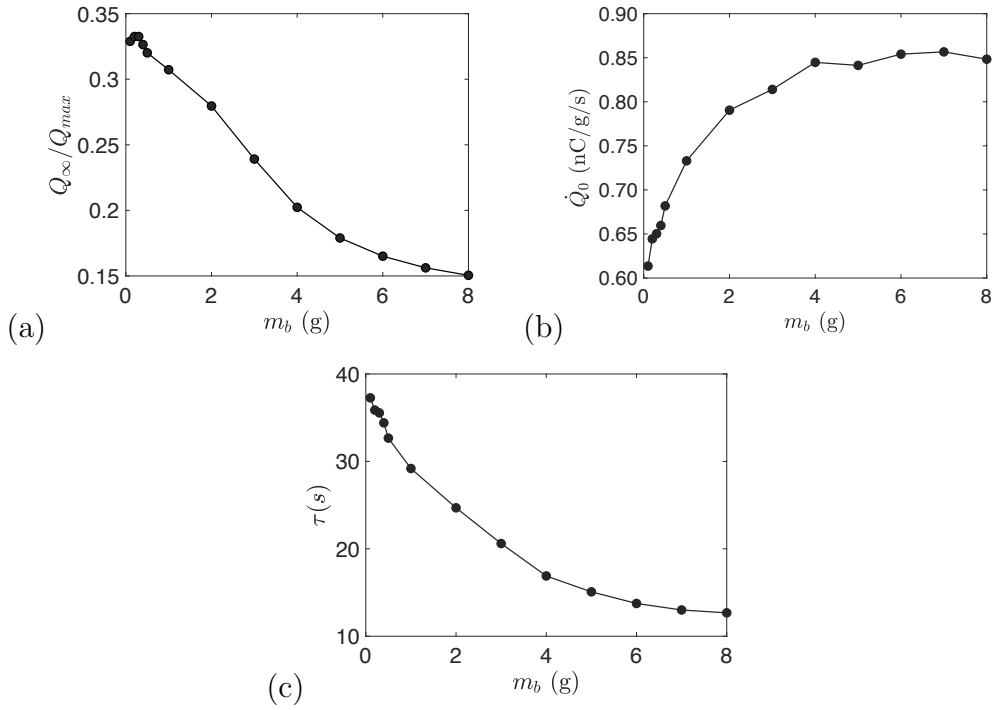

Figure 12: Asymptotic specific charge (a), initial charging rate $\dot{Q}_0$ (b), and characteristic time τ (c) as a function of bed mass m_b.

occurs at $m_b \simeq 5$ g above which $\dot{Q}_0$ remains constant. Fig. 12(c) shows the characteristic time τ as a function of m_b. It declines and tends to a constant value at highest values of m_b.

This evolution of the charging characteristics reflects the dynamics of collisions with the vibrating plate, which is at the origin of particle charging due to charge transfer. At the same time, particle-particle collisions tend to redistribute charges among particles by charge relaxation mechanism, but they have no effect on the total charge. The overall behavior depends therefore on the particle bed mass, which affects the balance of the two types of collisions and the amount of charge transfer and charge relaxation during each collision. To quantify these processes, we focus here on the collision rates and the transferred charges for each type of collision.

Figure 13(a) shows the evolution of the rates N_{pp} and N_{pw} of particle-particle and particle-plate collisions, respectively. Both N_{pp} and N_{pw} increase almost quadratically with m_b due to the increase of the total number of

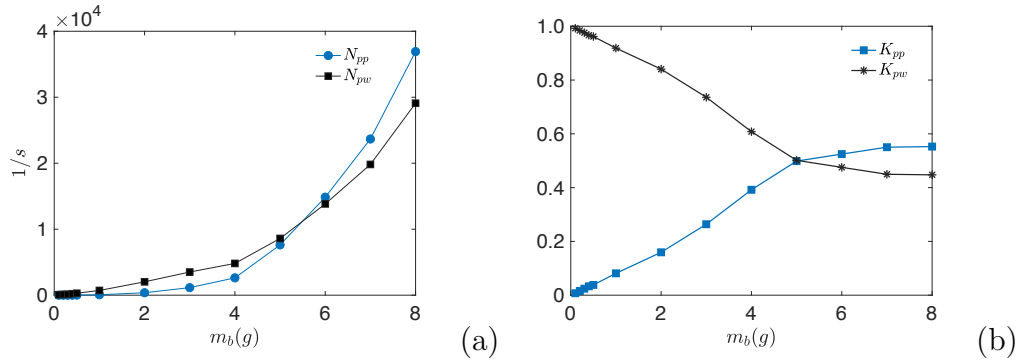

Figure 13: (a) Rates of collisions N_{pp} and N_{pw} between particles and with the vibrating plate, respectively, averaged over the whole period of vibration as a function of bed mass m_b; (b) Average relative rates K_{pp} and K_{pw} of particle-particle and particle-wall collisions as a function of bed mass m_b.

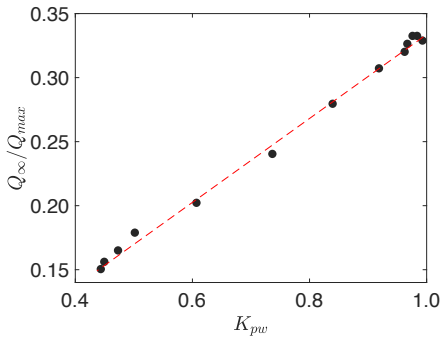

Figure 14: Correlation between saturation specific charge Q_∞ normalized by Q_{max} and the relative collision rate K_{pw} between particles and vibrating plate.

particles. Since the collision rates depend on bed mass while the specific electric charge acquired by the bed is described per unit mass, it is more convenient to consider the 'relative rates' defined by

$$\begin{aligned} K_{pp} &= \frac{N_{pp}}{N_{pp}+N_{pw}} \\ K_{pw} &= \frac{N_{pw}}{N_{pp}+N_{pw}}. \end{aligned} \tag{14}$$

Figure 13(b) displays K_{pp} and K_{pw} as a function of m_b. We see that particle-plate collisions prevail at low bed mass, but K_{pw} declines as m_b increases and beyond $m_b = 5$ g, K_{pp} slightly exceeds K_{pw}. This transition is consistent

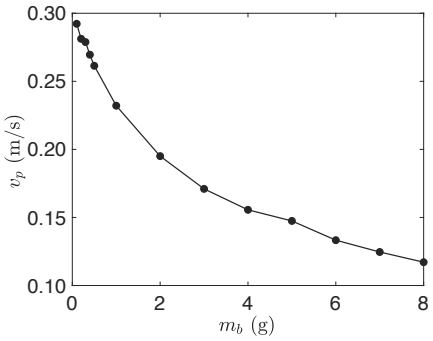

Figure 15: Relative velocity v_p averaged over the whole vibration period as a function of m_b.

with that observed in Fig. 12(b). It is physically plausible since the number of particles that can interact with the vibrating plate per unit time is increasingly inhibited by collisions between particles as the total number of particles increases. Interestingly, the decrease of K_{pw} with increasing m_b is also linearly correlated with Q_∞ as displayed in Fig. 14:

$$\frac{Q_\infty}{Q_{max}} \simeq 0.33 K_{pw} \tag{15}$$

In other words, lower values of the saturation specific charge correspond to lower values of K_{pw} for larger values of m_b. The total saturation charge varies therefore as $Q_\infty m_b = 0.33 Q_{max} K_{pw} m_b$.

It is also noteworthy that the average relative velocity v_p between particles and between particles and the vibrating plate declines with increasing m_b due to enhanced dissipation by inelastic collisions as shown in Fig. 15. Hence, we have two contradictory mechanisms that affect the charge transfer during collisions. The increase of N_{pw} implies more charge transfer whereas the decrease of v_p leads to lower transfer of charge at each collision with the plate.

Figure 16(a) shows the average value $\Delta Q^t_{pw_b}$ of the charge transferred in a collision between a particle and the vibrating plate (bottom wall) as a function of time for different values of bed mass m_b. The average charge per collision is calculated over a mobile time interval of 3 seconds. We see that $\Delta Q^t_{pw_b}$ reaches a constant value in a short time interval and its steady-state value declines as m_b increases. This is consistent with the decrease of the relative velocity v_r with increasing m_b due to increased dissipation as

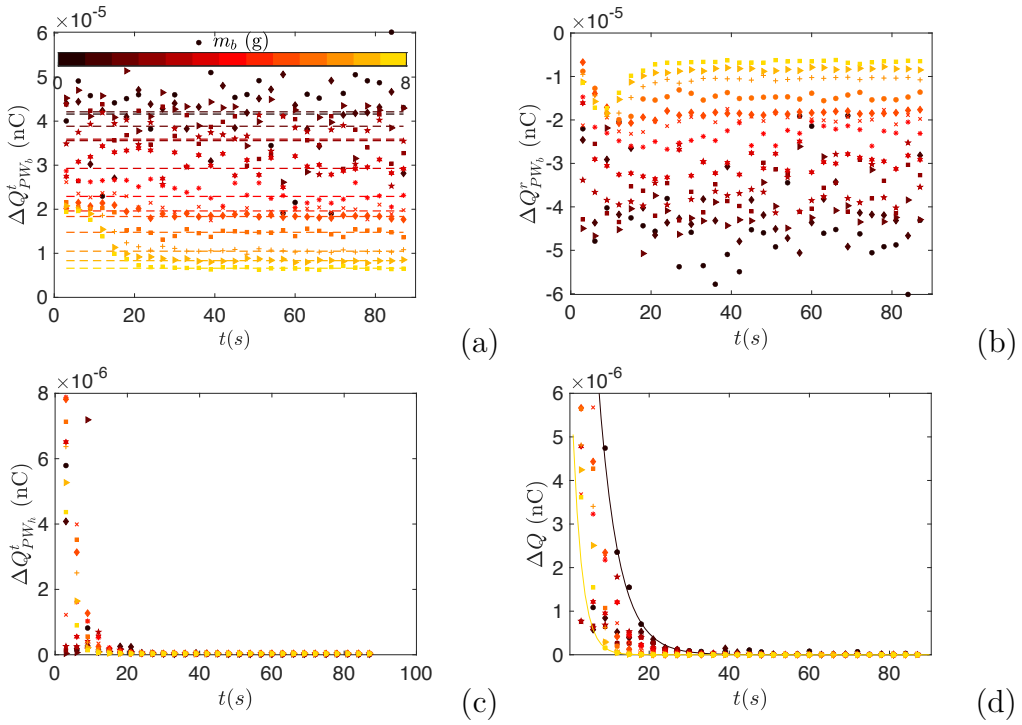

Figure 16: (a) Average charge $\Delta Q^t_{pw_b}$ transferred per collision between particles and the vibrating plate, (b) Average charge loss $\Delta Q^r_{pw_b}$ per collision between the particles and the vibrating plate due to charge relaxation, (c) average charge $\Delta Q^t_{pw_h}$ transferred per collision between particles and the lateral walls, and (d) total transferred charge per collision between particles for different values of bed mass m_b as a function of time. The solid lines in (d) are exponential fitting functions to the data points for the largest and smallest values of m_b.

observed in Fig. 15. This gain of charge is reduced on average by an amount equal to $\Delta Q^r_{pw_b}$ due to relaxation. Figure 16(b) shows $\Delta Q^r_{pw_b}$ as a function of time. The variation of $\Delta Q^r_{pw_b}$ in absolute value with time is similar to that of $\Delta Q^t_{pw_b}$. The net amount of charge gained by a particle varies therefore as $\Delta Q_{pw_b} = \Delta Q^t_{pw_b} + \Delta Q^r_{pw_b}$.

In the same way, the collisions with the lateral walls lead to an average gain of charge per collision $\Delta Q_{pw_h} = \Delta Q^t_{pw_h} + \Delta Q^r_{pw_h}$ by particle due to charge transfer $\Delta Q^t_{pw_h}$ and loss of charge $\Delta Q^r_{pw_h}$ by relaxation. Figure 16(c) displays $\Delta Q^t_{pw_h}$ as a function time. It shows that charge transfer at the lateral walls is an order of magnitude below that at the vibrating plate due to the much lower values of relative velocity at the lateral walls. Furthermore, this transfer occurs only during the transient (at most 20 s) and then drops to zero. Hence, the total average charge gained by a particle per collision ΔQ can be approximated by

$$\Delta Q \simeq \Delta Q_{pw_b} \simeq \Delta Q^t_{pw_b} + \Delta Q^r_{pw_b}. \tag{16}$$

Figure 16(d) shows ΔQ as a function time. We see that ΔQ is initially high, but falls off and vanishes in finite time in the steady state as a result of balance between gain by collisions with the vibrating plate and loss by relaxation. This falloff is exponentially fast as shown by the fits to the data for smallest and largest bed masses m_b in Fig. 16(d). The faster decrease of ΔQ with increasing m_g is consistent with the observed increase of $\dot{Q}_0$ in Fig. 12 as a function of m_b. During the transient time τ, we have

$$\dot{Q}_0 = \frac{1}{m_b \tau} \int_0^\tau N_{pw}(t) \Delta Q(t)\ dt. \tag{17}$$

Hence, the faster increase of N_{pw}/m_b overcompensates the decrease of ΔQ with increasing bed mass and leads to the increase of $\dot{Q}_0$ with m_b.

5. Scaling of charging kinetics

The evolution of specific charge Q with time in Fig. 11 shows that both the charging time τ and the saturation specific charge Q_∞ depend on the bed mass. In the last section, it was shown that this evolution is mainly controlled by the collisional dynamics of the granular bed. This suggests that the underlying charging process is similar for all values of the bed mass. This implies that the data must be scalable by normalizing the specific charge

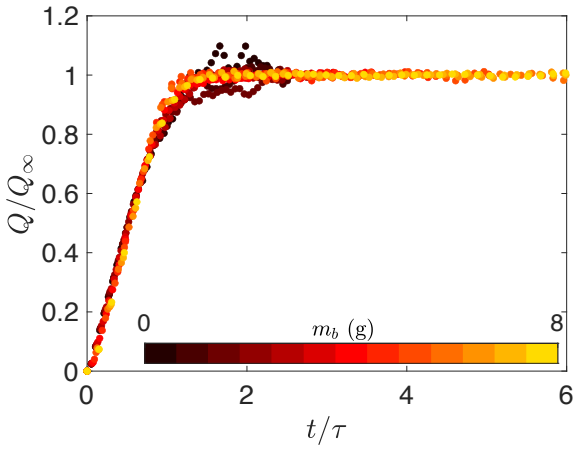

Figure 17: Specific charge Q normalized by saturation specific charge Q_∞ as a function of time t normalized by characteristic time τ for all values of bed mass m_b.

by Q_∞ and the time t by τ. Figure 17 shows that the normalized data do collapse on a master curve. This scaling does not fully capture the crossover from the nearly linear regime of rising charge to the saturation charge, which occurs at time $t \simeq \tau$, but, given the low number of simulated particles, it is remarkably good.

According to Eq. (15), the decrease of Q_∞ towards a constant value with increasing bed mass is correlated with that of the relative rate of collisions K_{pw} between the particles and the vibrating plate. However, the physical origin of the rise time τ is not obvious. We introduce here a simple model to quantify the time scales involved in the vibrated bed. Fig. 18 displays a snapshot of particles and their color-encoded charges after 20 s of vibration. We see that, although the particles collide both with the bottom plate and with other particles, the packing fraction is low. Hence, we assume that the dynamics is essentially collisional (for the values of vibration frequency and amplitude used in our simulations). We consider therefore the dynamics of a single particle and we account for collisions with other particles by introducing an effective restitution coefficient.

For a plate vibrating vertically with amplitude A and frequency $\omega = 2\pi\nu$, the contact of the particle with the plate opens only if $a\omega^2 > g$. When this condition is fulfilled, the velocity of the particle initially placed on the vibrating plate at the separation time is $v_0 = A\omega$. The particle rises while decelerating, reaches its highest position ΔH, and falls back into the plate

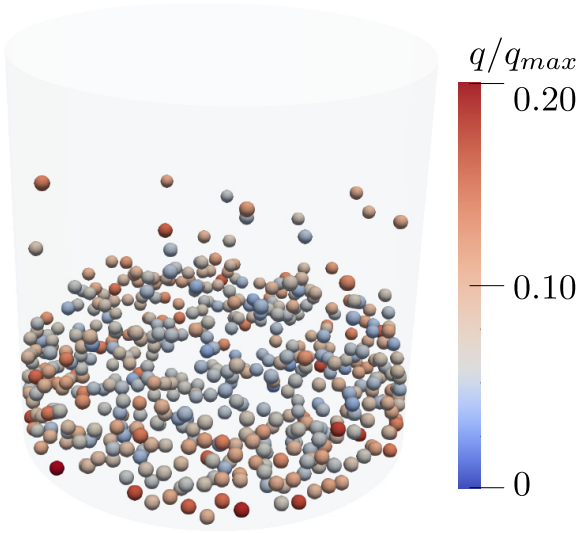

Figure 18: Snapshot of a triboelectrically charged layer of particles after a vibration time $t_v = 20$ s. Color level is proportional to particle charge.

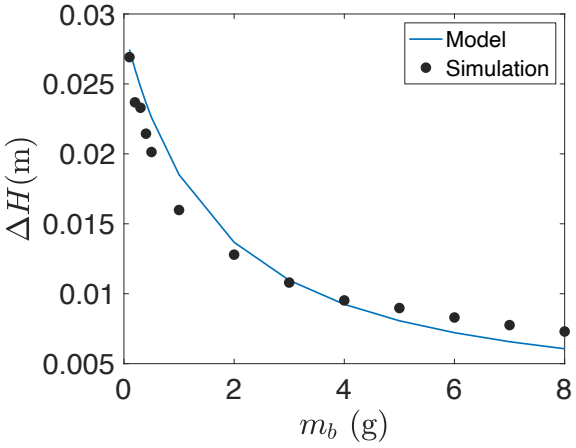

Figure 19: Bed height expansion ΔH as a function of bed mass m_b from simulations and model.

with a velocity v_0. The collision with the plate may occur while the plate is moving upward or downward. However, the largest relative impact velocity $2v_0$ occurs if the particle hits the plate while the latter is at its maximum upward velocity v_0. We assume that this is the case in order to calculate the maximum possible height of the particle. Given the restitution coefficient e_p between the particle and the plate, the relative velocity after the impact is $2v_0e_p$ and the velocity in the laboratory frame is $2v_0e_p + v_0$. More generally, the velocity v_k (in the laboratory frame) of the particle at the separation time after k impacts is given by

$$v_k = (v_0 + v_{k-1})e_p + v_0, \tag{18}$$

where v_{k-1} is the particle velocity at impact $k-1$. By iterating this relation, we obtain the following expression for the particle velocity:

$$v_k = \frac{1 + e_p - 2e_p^{k+1}}{1 - e_p} v_0. \tag{19}$$

Hence, since e_p^{k+1} tends to zero with k, the largest steady-state velocity is

$$v_{max} = A\omega \frac{1 + e_p}{1 - e_p}. \tag{20}$$

As a result, the corresponding maximum height reached by the particle is

$$\Delta H = \frac{v_{max}^2}{2g} = \frac{A^2\omega^2}{2g} \left(\frac{1 + e_p}{1 - e_p} \right)^2. \tag{21}$$

Figure 19 shows the increase $\Delta H = H - H_0$ of the bed height H from its initial height H_0 as a function of bed mass m_b. For the lowest mass $m_b = 0.1$ g, where the bed contains only a single dilute layer of particles, ΔH is nearly equal to the value ($\simeq 0.029$ m) given by Eq. (21) for the numerical values of $A = 1.5 \times 10^{-3}$ m, $\omega = 2\pi\nu$ with $\nu = 20$ Hz, g, and $e_p = 0.6$ used in the simulations. This indicates that single-particle assumption is relevant in the limit of low bed mass. However, ΔH declines as m_b increases. This decrease is obviously due to energy dissipation by multiple particle collisions. A simple way to account for this additional dissipation (in addition to dissipation due to incomplete restitution at the vibrating plate) consists in keeping the expression (21) but replacing the restitution coefficient e_p by a 'collective'

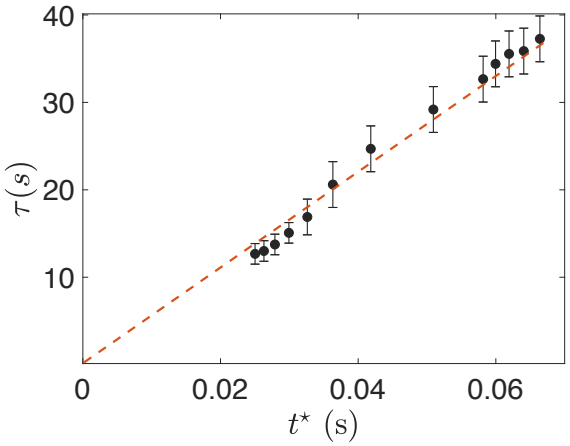

Figure 20: Characteristic charging time τ verus ballistic time t^* in simulations for all values of the bed mass. The errors bars represent the interval of confidence for the estimation of the charging time up to the steady state.

restitution coefficient e_c as a decreasing function of m_b. We postulate the following form

$$e_c = e_p(1 + m_b/m_0)^{-\alpha}, \tag{22}$$

where m_0 is a characteristic mass and $\alpha > 0$ is a parameter depending on the dynamics. This collective restitution coefficient is equal to e_p when $m_b \ll m_0$ and tends to zero when $m_b \gg m_0$. Hence, the bed expansion can be expressed as

$$\Delta H(m_b) = \frac{A^2\omega^2}{2g}\left\{\frac{1 + e_p(1 + m_b/m_0)^{-\alpha}}{1 - e_p(1 + m_b/m_0)^{-\alpha}}\right\}^2. \tag{23}$$

This expression is used in Fig. 19 to fit the simulation data. We see that the fit closely follows the data points with $m_0 = 5$ g and $\alpha = 0.75$.

With this 'calibration' of the expression of $\Delta H(m_b)$ from simulation data, we also can express the ballistic time t_b, i.e. the time taken by the particle to fall a distance $\Delta H(m_b)$:

$$t_b = \frac{v_{max}}{g} = \left(\frac{2\Delta H}{g}\right)^{1/2} = \frac{A\omega}{g}\frac{1 + e_c}{1 - e_c}. \tag{24}$$

Since the onset of fluidization implies the condition $A\omega^2 > g$, we have $A\omega/g > 1/\omega$. Hence, the minimum value of t_b occurs for $e_c = 0$ (infinite mass):

$$t_{bmin} = \frac{1}{\omega}. \tag{25}$$

We can therefore define a time scale t^* of fluidization by subtracting t_{bmin} from t_b:

$$t^*(m_b) = \frac{A\omega}{g}\frac{1+e_p(1+m_b/m_0)^{-\alpha}}{1-e_p(1+m_b/m_0)^{-\alpha}} - \frac{1}{\omega}. \tag{26}$$

Figure 20 shows the characteristic time τ versus t^* with $\alpha = 0.75$ and $m_0 = 5$ g for all values of the bed mass. We see that τ is proportional to t^* with a prefactor $\simeq 580$. This means that, for all values of m_b, the time required for the charging of the particles up to the saturation value corresponds to an average number of 290 collisions of each particle with the vibrating plate. Note that the total ballistic time of a particle (rise and fall) is $2t^*$. Indeed, we expect that this number is equal to $\tau N_{pw}/N_p$, where N_p is the number of particles. For example, for $m_b = 8$ g, this ratio (with $\tau \simeq 10$ s, $N_{pw} = 3 \times 10^4$ s^{-1}, and $N_p = 1000$) is 300, which is very close to the above value calculated from the proportionality between τ and t^*. The scaling of τ by t^* suggests that the decrease of charging time with bed mass reflects the decrease of ballistic time. This assertion needs, however, further validation by means of simulations of charging for different values of vibration amplitude and frequency.

6. Conclusion

In this study, we employed a combination of particle dynamics simulations and experiments to explore the charging kinetics of a granular bed within a vibrating cell. Our approach involved developing a triboelectric charging model, incorporating a relaxation term, and conducting extensive charging simulations for granular beds with varying mass. To validate our numerical model, we calibrated its parameters through charging experiments using glass beads on a vibrating polypropylene plate. Remarkably, our simulation results for specific charge over time aligned well with experimental data across multiple bed masses. We used the simulations to analyze the charging process by considering the collision rates, relative velocities, and the transfer and relaxation of charges per particle.

A key observation was that the specific charge per unit mass increased with time before stabilizing at a constant value. This saturation was attributed to a balance between charge transfer from collisions with the vibrating plate and charge relaxation. Interestingly, the data showed also that saturation specific charge decreased with increasing bed mass due to a reduction in the relative collision rate between particles and the plate compared to

inter-particle collisions. Another important observation was that the charging characteristic time decreased with higher bed masses. We introduced a simple model based on single-particle dynamics, accurately predicting bed expansion with a restitution coefficient dependent on bed mass. This model further forecasted a diminishing ballistic time in relation to particle mass, with the charging characteristic time effectively scaled by this ballistic time within the studied bed mass range. Due to the underlying dynamics of the charging process, our simulation data for specific charge over time remarkably collapsed onto a single master curve when specific charges were normalized by the saturation charge, and times were normalized by the characteristic time.

The numerical model developed in this study has the potential for application in exploring charging kinetics for larger bed masses, varying vibration amplitudes and frequencies, and different particle-plate restitution coefficients. Future investigations should assess the model's validity under different vibration conditions and explore its efficiency for simulating larger particle numbers. This expansion could provide insights into how particle dynamics and charging physics depend on system size.

7. Acknowledgment

This work has been realized with the support of MESO@LR-Platform at the University of Montpellier. The authors also thank the PLANET facility (DOI: 10.15454/1.5572338990609338E12) run by the IATE joint research unit for providing process experiment supports.

References

[1] L.-H. Lee, Adhesion and cohesion mechanisms of lunar dust on the moon's surface, Journal of Adhesion Science and Technology 9 (8) (1995) 1103–1124. doi:10.1163/156856195X00932.

[2] H. Kawamoto, S. Hashime, Practical performance of an electrostatic cleaning system for removal of lunar dust from optical elements utilizing electrostatic traveling wave, Journal of Electrostatics 94 (2018) 38–43. doi:https://doi.org/10.1016/j.elstat.2018.05.004.

[3] M. Glor, Electrostatic ignition hazards in the process industry, Journal of Electrostatics 63 (6) (2005) 447–453, 10th International Conference on Electrostatics. doi:https://doi.org/10.1016/j.elstat.2005.03.001.

[4] M. Bailey, P. Hooker, P. Caine, N. Gibson, Incendivity of electrostatic discharges in dust clouds: the minimum ignition energy problem, Journal of Loss Prevention in the Process Industries 14 (2) (2001) 99–101. doi:https://doi.org/10.1016/S0950-4230(00)00030-9.

[5] R. Gupta, D. Gidaspow, D. Wasan, Electrostatic separation of powder mixtures based on the work functions of its constituents, Powder Technology 75 (1) (1993) 79 – 87. doi:https://doi.org/10.1016/0032-5910(93)80027-8.

[6] J. Landauer, P. Foerst, Triboelectric separation of a starch-protein mixture – impact of electric field strength and flow rate, Advanced Powder Technology 29 (1) (2018) 117 – 123. doi:https://doi.org/10.1016/j.apt.2017.10.018.

[7] Q. Yang, J. Chen, X. Zhou, H. Zhou, G. Yang, J. Zhu, Modeling of inter-tablet coating uniformity of electrostatic dry powder coating by discrete element method, Powder Technology 411 (2022) 117929. doi:https://doi.org/10.1016/j.powtec.2022.117929.

[8] J. Vanamu, A. Sahoo, An overview on dry powder coating in advancement to electrostatic dry powder coating used in pharmaceutical industry, Powder Technology 399 (2022) 117214. doi:https://doi.org/10.1016/j.powtec.2022.117214.

[9] D. A. Hays, Paper documents via the electrostatic control of particles, Journal of Electrostatics 51-52 (2001) 57–63, electrostatics 2001: 9th International Conference on Electrostatics. doi:https://doi.org/10.1016/S0304-3886(01)00096-1.

[10] C. H. Park, J. K. Park, H. S. Jeon, B. C. Chun, Triboelectric series and charging properties of plastics using the designed vertical-reciprocation charger, Journal of Electrostatics 66 (11) (2008) 578–583. doi:https://doi.org/10.1016/j.elstat.2008.07.001.

[11] K. Zhu, S. M. Rao, Q. H. Huang, C.-H. Wang, S. Matsusaka, H. Masuda, On the electrostatics of pneumatic conveying of granular materials using electrical capacitance tomography, Chemical engineering science 59 (15) (2004) 3201–3213.

[12] P. Mehrani, H. T. Bi, J. R. Grace, Electrostatic charge generation in gas–solid fluidized beds, Journal of electrostatics 63 (2) (2005) 165–173.

[13] C.-C. Liao, S.-S. Hsiau, T.-Y. Huang, The effect of vibrating conditions on the electrostatic charge in a vertical vibrating granular bed, Powder technology 208 (1) (2011) 1–6.

[14] M. Yoshida, N. Ii, A. Shimosaka, Y. Shirakawa, J. Hidaka, Experimental and theoretical approaches to charging behavior of polymer particles, Chemical Engineering Science 61 (7) (2006) 2239 – 2248, papers Presented at the Eleventh and Twelfth Nisshin Engineering Particle Technology International Symposium. doi:https://doi.org/10.1016/j.ces.2004.06.052.

[15] J. Cross, Electrostatics, principles, problems and applications, CRC Press, 1987.

[16] Y. Shi, M. Fang, Q. Wang, K. Yan, J. Cen, W. Zeng, Z. Luo, Numerical study of the effect of temperature and h2o concentration on the electrostatic precipitator characteristics at high temperatures, Powder Technology (2022) 117913doi:https://doi.org/10.1016/j.powtec.2022.117913.

[17] O. Tilmatine, T. Zeghloul, K. Medles, L. Dascalescu, A. Fatu, Effect of ambient air relative humidity on the triboelectric properties of polypropylene and polyvinyl chloride slabs, Journal of Electrostatics 115 (2022) 103651. doi:https://doi.org/10.1016/j.elstat.2021.103651.

[18] J. Kolehmainen, P. Sippola, O. Raitanen, A. Ozel, C. M. Boyce, P. Saarenrinne, S. Sundaresan, Effect of humidity on triboelectric charging in a vertically vibrated granular bed: Experiments and modeling, Chemical Engineering Science 173 (2017) 363–373. doi:https://doi.org/10.1016/j.ces.2017.08.006.

[19] Y. Cheng, L. Lee, W. Zhang, C. Wang, Investigation on electrostatic charging and its effect on mixing of binary particles in a vibrating bed, Industrial & Engineering Chemistry Research 53 (2014) 14166–14174.

[20] H. Grosshans, M. V. Papalexandris, A model for the non-uniform contact charging of particles, Powder Technology 305 (2017) 518–527. doi:https://doi.org/10.1016/j.powtec.2016.10.024.

[21] C. Gallo, W. Lama, Some charge exchange phenomena explained by a classical model of the work function, Journal of Electrostatics 2 (2) (1976) 145–150.

[22] T. Matsuyama, H. Yamamoto, Charge relaxation process dominates contact charging of a particle in atmospheric conditions, Journal of Physics D: Applied Physics 28 (12) (1995) 2418–2423. doi:10.1088/0022-3727/28/12/005.

[23] W. D. Greason, Investigation of a test methodology for triboelectrification, Journal of Electrostatics 49 (3-4) (2000) 245–256.

[24] J. Laurentie, P. Traoré, L. Dascalescu, Discrete element modeling of triboelectric charging of insulating materials in vibrated granular beds, Journal of Electrostatics 71 (6) (2013) 951 – 957. doi:https://doi.org/10.1016/j.elstat.2013.08.001.

[25] L.-S. Lu, S.-S. Hsiau, Mixing in vibrated granular beds with the effect of electrostatic force, Powder technology 160 (3) (2005) 170–179.

[26] M. D. Hogue, C. I. Calle, D. Curry, P. Weitzman, Discrete element modeling (dem) of triboelectrically charged particles: revised experiments, Journal of Electrostatics 67 (4) (2009) 691–694.

[27] S. Watano, S. Saito, T. Suzuki, Numerical simulation of electrostatic charge in powder pneumatic conveying process, Powder Technology 135-136 (2003) 112 – 117, electrostatic Phenomena in Particulate Processes. doi:https://doi.org/10.1016/S0032-5910(03)00159-1.

[28] T. Matsuyama, H. Yamamoto, Charge transfer between a polymer particle and a metal plate due to impact, IEEE Transactions on Industry Applications 30 (3) (1994) 602–607. doi:10.1109/28.293706.

[29] N. D. Lang, A. R. Williams, Theory of local-work-function determination by photoemission from rare-gas adsorbates, Phys. Rev. B 25 (1982) 2940–2942. doi:10.1103/PhysRevB.25.2940.

[30] O. Kwon, Y. Kim, Probing of surface potential using atomic force microscopy, Applied Microscopy 44 (3) (2014) 100–104.

[31] S. Matsusaka, H. Maruyama, T. Matsuyama, M. Ghadiri, Triboelectric charging of powders: A review, Chemical Engineering Science 65 (22) (2010) 5781 – 5807. doi:https://doi.org/10.1016/j.ces.2010.07.005.

[32] S. Matsusaka, M. Ghadiri, H. Masuda, Electrification of an elastic sphere by repeated impacts on a metal plate, Journal of Physics D: Applied Physics 33 (18) (2000) 2311. doi:10.1088/0022-3727/33/18/316.
URL https://dx.doi.org/10.1088/0022-3727/33/18/316

[33] H. Hertz, Ueber die berührung fester elastischer körper., Journal für die reine und angewandte Mathematik 92 (1882) 156–171.

[34] Z. Chen, F. Liu, L. Wang, Y. Li, R. Wang, Z. Chen, Tribocharging properties of wheat bran fragments in air–solid pipe flow, Food Research International 62 (2014) 262 – 271. doi:https://doi.org/10.1016/j.foodres.2014.03.006.

[35] D. B. Go, D. A. Pohlman, A mathematical model of the modified paschen's curve for breakdown in microscale gaps, Journal of Applied Physics 107 (10) (2010) 103303. arXiv:https://doi.org/10.1063/1.3380855, doi:10.1063/1.3380855.

[36] F. Radjai, F. Dubois, Discrete-element modeling of granular materials, Wiley-Iste, 2011.

[37] S. Luding, Introduction to discrete element methods, European Journal of Environmental and Civil Engineering 12 (7-8) (2008) 785–826. doi:10.1080/19648189.2008.9693050.

[38] C. O'Sullivan, Particulate Discrete Element Modelling: A Geomechanics Perspective, Taylor & Francis, 2011.

[39] M. P. Allen, D. J. Tildesley, Computer simulation of liquids, Oxford university press, 2017.

[40] V. Richefeu, Approche par éléments discrets 3d du comportement de matériaux granulaires cohésifs faiblement contraints, Ph.D. thesis, Université Montpellier II-Sciences et Techniques du Languedoc (2005).

[41] J. M. Ting, B. T. Corkum, Computational laboratory for discrete element geomechanics, Journal of computing in civil engineering 6 (2) (1992) 129–146.

[42] S. Pan, Z. Zhang, Fundamental theories and basic principles of triboelectric effect: A review, Friction 7 (1) (2019) 2–17. doi:10.1007/s40544-018-0217-7.

[43] H. Zou, Y. Zhang, L. Guo, P. Wang, X. He, G. Dai, H. Zheng, C. Chen, A. C. Wang, C. Xu, Z. L. Wang, Quantifying the triboelectric series, Nature Communications 10 (1) (2019) 1427.

[44] D. J. Lacks, R. M. Sankaran, Contact electrification of insulating materials, Journal of Physics D: Applied Physics 44 (45) (2011) 453001.

[45] A. Lorenz, C. Tuozzolo, M. Louge, Measurements of impact properties of small, nearly spherical particles, Oceanographic Literature Review 3 (45) (1998) 603.

[46] H. Tang, R. Song, Y. Dong, X. Song, Measurement of restitution and friction coefficients for granular particles and discrete element simulation for the tests of glass beads, Materials 12 (19) (2019).

[47] S. Naik, R. Mukherjee, B. Chaudhuri, Triboelectrification: A review of experimental and mechanistic modeling approaches with a special focus on pharmaceutical powders, International Journal of Pharmaceutics 510 (1) (2016) 375 – 385. doi:https://doi.org/10.1016/j.ijpharm.2016.06.031.

[48] A. Lorenz, C. Tuozzolo, M. Y. Louge, Measurements of impact properties of small, nearly spherical particles, Experimental Mechanics 37 (1997) 292.

[49] H. Tang, R. Song, Y. Dong, X. Song, Measurement of restitution and friction coefficients for granular particles and discrete element simulation for the tests of glass beads, Materials 12 (2019).

[50] I. Olefins, P. USA, Typical Engineering Properties of Polypropylene, www.ineos-op.com (2014).

[51] S. Naik, S. Sarkar, V. Gupta, B. C. Hancock, Y. Abramov, W. Yu, B. Chaudhuri, A combined experimental and numerical approach to explore tribocharging of pharmaceutical excipients in a hopper chute assembly, International journal of pharmaceutics 491 (1-2) (2015) 58–68.

[52] N. Duff, D. J. Lacks, Particle dynamics simulations of triboelectric charging in granular insulator systems, Journal of Electrostatics 66 (1-2) (2008) 51–57.

[53] J. Kolehmainen, A. Ozel, C. M. Boyce, S. Sundaresan, Triboelectric charging of monodisperse particles in fluidized beds, AIChE Journal 63 (6) (2017) 1872–1891.